Novel transmitter designs for magnetic resonance imaging

Aussenhofer, S.A.

4

AN EIGHT-CHANNEL TRANSMIT/RECEIVE ARRAY OF TE_{01} MODE HIGH PERMITTIVITY CERAMIC RESONATORS FOR HUMAN IMAGING AT 7.0 TESLA.

Sebastian A. AUSSENHOFER

Andrew G. WEBB

Parts of this chapter have been published in Magnetic resonance in medicine: official journal of the Society of Magnetic Resonance in Medicine **68**, 1325-31 (2012) [2].

4

This study describes the design, construction and operation of a new type of transmit/receive array using ceramic resonators operating in a transverse electromagnetic (TE) mode. Single element function and performance at 298.1MHz (7.0 Tesla) are analyzed and compared to a lumped element design loop coil with comparable geometry. The results show that ceramic resonators working in the $TE_{01\delta}$ mode configuration produce similar efficiency, defined as the transmit magnetic field B_1^+ per square root of the specific absorption rate (SAR), to conventional surface coils. An array consisting of eight ceramic elements was then designed to operate in transmit/receive mode. This array was driven via power/phase splitters by two independent transmit channels and functional cardiac images were produced from a number of healthy volunteers.

4.1. INTRODUCTION

DUE to the intrinsic wavelength effects at very high frequency (VHF), and the lack of a homogenous excitation source such as the body coil on 3 T systems, resonator design for VHF-MR body imaging requires transmit or transceiver arrays. A variety of different designs have been suggested, including microstrip elements [11, 15, 20], radiative antennas [13], and loop coils [4, 5, 17]. Sophisticated arrays of up to 32 elements have been produced, and the quality of body images at 7.0 T and above continues to improve. Nevertheless,there is currently no general consensus on the best type of resonator to use, and the area remains open to new types of design.

An alternative design, explored here for the first time, is to use dielectric resonator antennas (DRAs) made from very high permittivity materials. The concepts of both resonant [1, 2, 8] and non-resonant [10] high-permittivity structures have been used in recent high field design. Following initial work by Wen et al. [24], it has been shown that numerous modes of a resonant cavity can, in principle, be used for imaging [23]. In this current work we investigate a new application of cylindrical DRAs made from high permittivity, low loss ceramics for forming a transceiver array for body imaging at 7 T. These are designed to operate in the $TE_{01\delta}$ mode [8, 23, 24]. Their performance is compared to that of an identically-sized segmented loop coil in terms of magnetic and electric field distributions, and transmit efficiency. In addition to electromagnetic (EM) simulations and phantom experiments, preliminary experiments using an eight-element transmit/receive array have been performed in cardiac imaging, since this forms one of the major applications at high field [4–6, 12, 14, 17–22, 25]. As has been pointed out by Niendorf et al. [12] the promise of enhanced relative spatial resolution could enable new myocardial tissue characterization as well as micro-structural investigation.

4.2. MATERIALS AND METHODS

4.2.1. DESIGN OF INDIVIDUAL CERAMIC RESONATORS

In order to design a ceramic disk whose $TE_{01\delta}$ mode is resonant at 298 MHz calculations of appropriate dimensions and dielectric constant were carried out using the formula published by Kajfez and Gullion [9]:

$$f_{TE_{01\delta}} = 2.921 \frac{c\epsilon_r^{-0.465}}{2\pi a}\left[0.691 + 0.319\frac{a}{h} - 0.035\left(\frac{a}{h}\right)^2\right] \tag{4.1}$$

where $f_{TE01\delta}$ is the frequency of the $TE_{01\delta}$ mode in MHz, a the radius and h the height of the resonator (both in cm), c the speed of light and ϵ_r the relative permittivity. While this formula gives a good starting point, detailed EM simulations (see below) were carried out to refine the structure before production. A set of $BaSrTiO_3$ resonators with a relative permittivity of 165, designed to be shielded on top with a copper disk, was obtained from TCI Ceramics Inc. (Bethlehem, PA). A height of 39 mm and radius of 43 mm resulted in a resonance frequency of the TE_{01} mode at 270 MHz, which could then be fine tuned to 298 MHz by changing the distance between the coplanar copper shield and the resonator. A photograph of a single resonator is shown in Fig. 4.1(a).

For impedance matching and coupling energy into the ceramic resonator, inductive coupling via a small non-resonant coupling loop was used as shown in Fig. 4.1(b and c). Since large coupling loops would change the boundary condition on the coupling plane of the resonator the coupling loops were designed to be only 35 mm in outer diameter with a track thickness of 2 mm, etched on FR4 PC board The loops were place concentrically on the top side of the ceramic resonators as shown in Fig. 4.1(b) for maximum coupling to the TE mode. The loop was tuned to ~250 MHz by adjusting a variable capacitor (Voltronics, Salisbury, MD). A capacitive matching network consisting of two fixed capacitors (American Technical Ceramics, Huntington Station, NY) was adjusted to obtain critical coupling when loaded with the human body.

The eight element transmit/receive array design consisted of an anterior and posterior section, each comprising four individual housings, one for each element (Fig. 4.1(d)), that were manufactured on a 3D rapid prototyping machine (3D Touch, BitsfromBytes LCC). The position of the anterior elements can be altered with respect to one another, but the four resonators on the posterior side are fixed in place, as shown in Fig. 4.1(e).

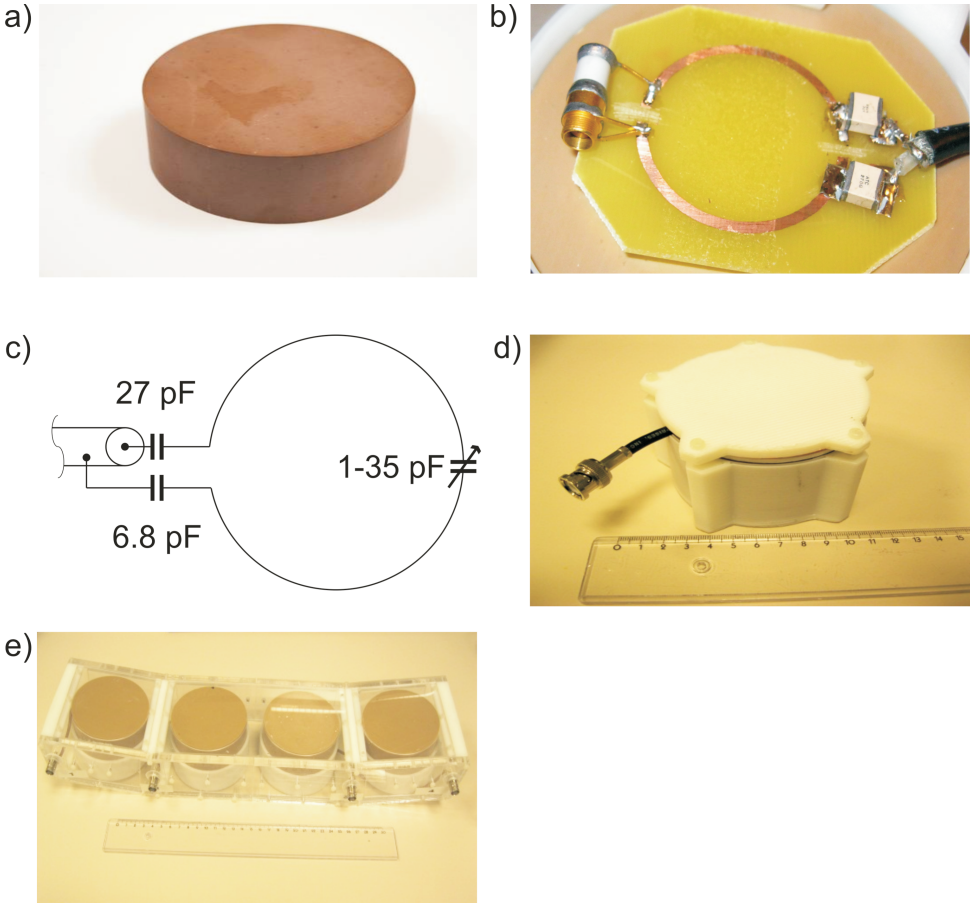

Figure 4.1: (a) shows a single ceramic resonator designed for TE_{01} mode excitation at 298 MHz made from $BaSrTiO_3$. The dimensions are diameter 86 mm and a height of 39 mm with a relative permittivity of 165. (b) Shows the coupling circuit etched on FR4 located on top of a ceramic resonator for impedance matching. (c) Shows the schematic for the coupling loops used for impedance matching. (d) Shows a single anterior element in a custom-built acrylonitrile butadiene styrene (ABS) housing that has a shield integrated into the top section. (e) Shows the posterior elements packed together into a conformal housing made from ABS and acrylic sheets.

4.2.2. REFERENCE LOOP COIL

In order to evaluate the performance of the TE_{01} mode resonators a circular loop coil was constructed for comparison. The coil had the same outer diameter of 8.6 cm with a track thickness of 5 mm and was split into eight segments of equal length. Eight capacitors (15 pF each) were distributed equally in the segment gaps in order to resonate the loop at 298 MHz. A conventional capacitive π-network was used for impedance matching.

4.2.3. ELECTROMAGNETIC SIMULATIONS

Simulations were performed with CST Microwave Studio version 2012 (CST AG, Darmstadt, Germany) on a workstation equipped with two Intel Xeon X5660 central processing units, 48 gigabytes of random access memory and two Nvidia Tesla C1060 graphic processing units (GPUs). Each simulation was set up with 20 lines per wavelength, a lower mesh limit of 10 and a mesh line ratio limit of 50 leading to a total of 47 million mesh cells. A full simulation took about 12 h to run with GPU acceleration computing. After the FDTD simulation all devices were matched to 50 Ω in the circuit simulator, and the fields were recalculated to take the matching into account. All simulations reached a convergence of ~50 dB: the ceramic resonators needed more simulation cycles than the loop coil due to the low loss of the ceramic substrate.

For phantom simulations the loop coil and the shielded ceramic resonator were placed on top of a cubic phantom with an edge length of 200 mm, relative permittivity of 78 and a conductivity of 0.5 Sm. Two distances (3 and 13 mm) between the bottom of the resonator and the phantom were evaluated. The reason to include two distances is that the dielectric resonator is ideally placed as close to the body as possible, whereas the loop coil (with its strong electric fields close to the segmenting capacitors) should be placed a small distance away from the body. An overview of the simulation setup for the single elements is given in Fig. 4.2. Lumped element losses were not included, which may lead to a slight overestimation of the efficiency of the loop coils.

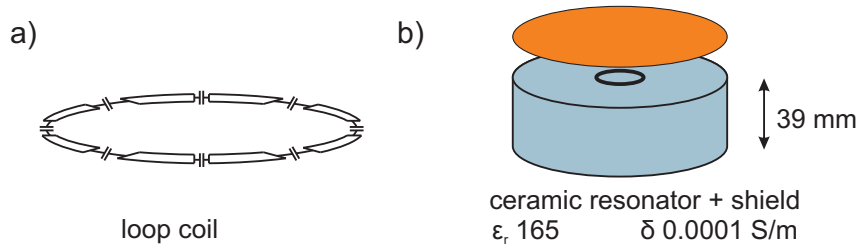

Figure 4.2: Setup of the single elements for the simulation. (a) Shows the surface loop coil capacitively segmented 8 times, (b) shows a ceramic resonator with a height of 39 mm height and a copper shield that is lowered towards the resonator until the TE_{01} mode is at 298 MHz.

Whole body simulations were performed on the virtual family member Gustav [3] positioned inside a metallic tube mimicking the bore of the 7 T MRI system. Eight dielectric resonators were placed anterior (four) and posterior (four) around the chest to evaluate the performance of the array in terms of B_1^+ transmit field and specific absorption rate (SAR). The position of the individual array elements on the chest of Gustav is given in Fig. 4.3. The same positions were used for simulations of both the DRAs and the loop coils.

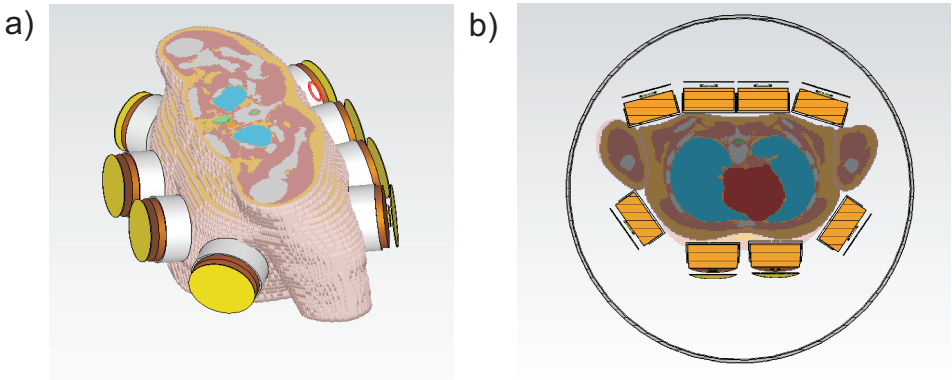

Figure 4.3: Positioning of the elements on the chest of the virtual family member Gustav. For the loop coil simulations the individual loop elements were placed concentric in plastic spacers with their bottom side coincident with the bottom part of the spacer.

4.2.4. HARDWARE SETUP AND CHARACTERIZATION

The Philips system is only equipped with two independent transmit channels, rather than the eight (or more) offered by other vendors. Each of the two channels was split into four channels with homebuilt power splitters (microstrip Wilkinson design) and fed through a homebuilt transmit/receive switch box. The insertion loss through the transmit chain was about 4.2 dB from amplifier to the single coil elements (~2.2 dB in terms of cable loss from RF amplifiers to the coil, and ~2.0 dB loss in the custom-built transmit/receive switches). In order to determine optimal (given the limitations of only two independent channels) phase differences between the upper four and lower four elements of the array, scout images were acquired with 0°, 90°,180° and 270° phase difference. These images were inspected to see which setting gave the least degree of signal voids (usually present as a distinct black band) through the heart. Much more sophisticated B_1-shimming algorithms exist on other commercial systems, but in this case our work was constrained by system hardware limitations. Different optimal phase settings were found for different subjects.

4.2.5. MRI ACQUISITION PROTOCOL AND PARAMETERS

The study adhered to the Leiden University Medical Center Institutional Review Board guidelines and informed consent was obtained from volunteers (N = 14) prior to the study. Phantom experiments used a large rectangular (360 × 200 × 180 mm) container filled with tissue-mimicking material (dielectric constant ~79 and conductivity ~0.5 S/m). B_1^+ mapping was performed using a dual TR method. In vivo experiments were conducted on a 7 T whole-body human scanner (Philips Achieva, Best, The Netherlands). Data obtained from the fourteen healthy volunteers, both male and female (seven each), used a cine sequence during consecutive breath-holds. The volunteers had a mean body mass index of 23.6 ± 7 and mean heart rate of 69 ± 10 beats per minute. Short axis views were obtained with the following parameters: retrospectively EKG triggered turbo field echo sequence with a field-of-view 300 mm (foot–head) × 295 mm (right–left) ×8 mm (anterior–posterior), spatial resolution 1.39 × 1.44 × 8 mm, TR/TE 4.0/2.5 ms, 33 cardiac phases, one breath-hold time 13.4 s per slice, thirteen slices, flip angle 8.5° and an average RF power of 23.5 W. The four-chamber view was acquired with the following parameters: retrospectively EKG triggered turbo field echo sequence with a field-of-view 380 mm (right–left) × 275 mm (anterior–posterior), spatial resolution 1.3 × 1.35 × 8 mm, single slice, TR/TE 4.23/ 2.5 ms, 33 cardiac phases, flip angle 8.5 degrees and an average RF power of 22.4 W. The two chamber view was obtained with the following parameters:

retrospectively EKG triggered turbo field echo sequence with a field-of-view 380 mm (right–left) × 275 mm (anterior–posterior), spatial resolution 1.3 × 1.35 × 8 mm, single slice, TR/TE 4.1/2.1 ms, 33 cardiac phases, flip angle 8.5 degrees and an average RF power of 23.5 W.

4.3. RESULTS

4.3.1. COIL CHARACTERIZATION

AFTER the assembly of the eight individual array elements, all elements were connected to a network analyzer for S-parameter characterization. A reflection coefficient (S_{11}) lower than –15 dB on all elements was measured when loaded with a human body. The plots for a resonator loaded with the human body, as well as that of an unloaded resonator (without any retuning of the impedance matching circuit) are given in Fig. 4.4.

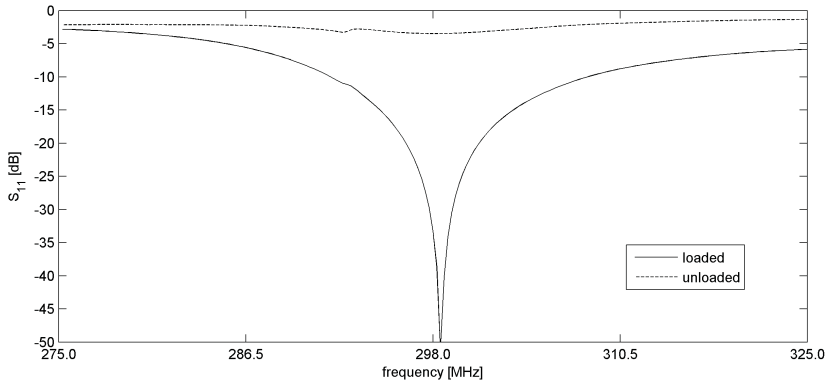

Figure 4.4: S_{11}-parameter plots of the loaded and unloaded shielded ceramic element in the eight-channel array. The data shown here were obtained from a volunteer with a high BMI > 30, the mean SS_{11} for three volunteers (low, medium and high BMI) was ~21.6 dB at 298.1 MHz with a standard deviation of 11.9 dB.

4.3.2. SINGLE ELEMENT ANALYSIS

The electric field and corresponding SAR distributions were examined first. All simulations were scaled to 1 W stimulated power and the IEEE C95.3 [7] averaging method was used to evaluate the 10 g average SAR ($SAR_{10g,avg}$). The IEEE C95.3 method uses a cube which is grown around the specific point P until it contains the required mass. Plots of the electric field and $SAR_{10g,avg}$ along the central plane through the phantom are shown in Fig 4.5.

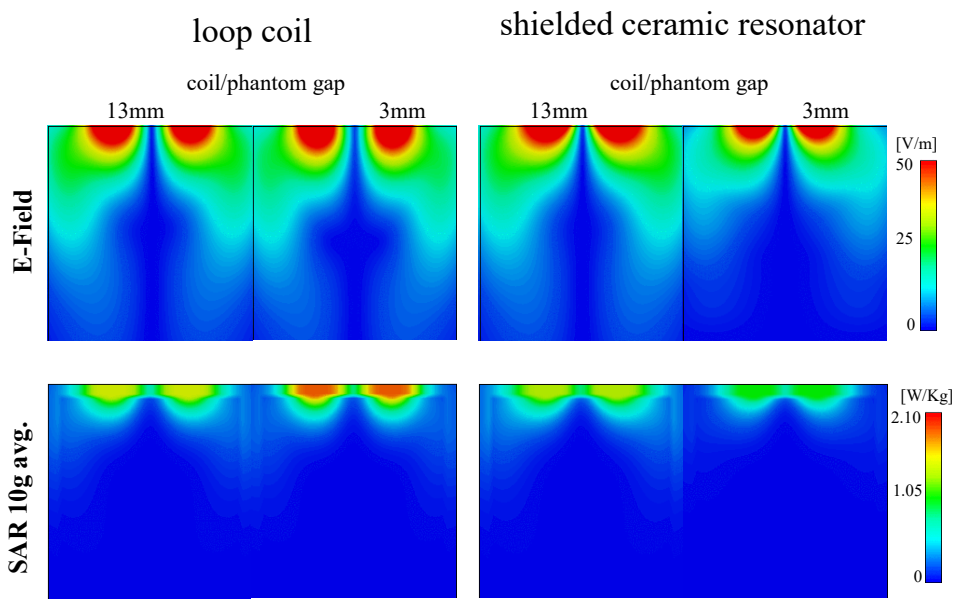

Figure 4.5: Top row: Electric field patterns for the loop coil and shielded dielectric resonator for 3 and 13 mm spacing between the phantom and coil. The bottom row gives the SAR_{10g} distribution for 3 and 13 mm spacing. All SAR plots are scaled to a maximum of 2.1 W/kg.

The simulations show that the general pattern of the electric field for both types of coil is very similar; in general the $SAR_{10g,avg}$ for the loop coil is higher compared to the shielded ceramic resonator. The SAR was also evaluated for the 1 g average (SAR_{1g}) according to the IEEE C95.3 averaging method, with results given in Table 4.1.

Table 4.1: Single element SAR analysis.

	3 mm gap between coil and phantom		13 mm gap between coil and phantom	
	SAR_{max} 10 g avg. (W/kg)	SAR_{max} 1 g avg. (W/kg)	SAR_{max} 10 g avg. (W/kg)	SAR_{max} 1 g avg. (W/kg)
Loop coil	2.06	3.54	1.54	2.29
Shielded ceramic resonator	1.79	2.76	1.40	2.03

The B_1^+ for 1 W input power (rms) and the $B_1^+/\sqrt{SAR_{10g,max}}$ were also evaluated in the same plane and the plots are given in Fig. 4.6. Here the elements all perform quite similarly. Experimental B_1^+ maps obtained with the dual-TR method, also shown in Fig. 4.6, confirm the general pattern from the simulations.

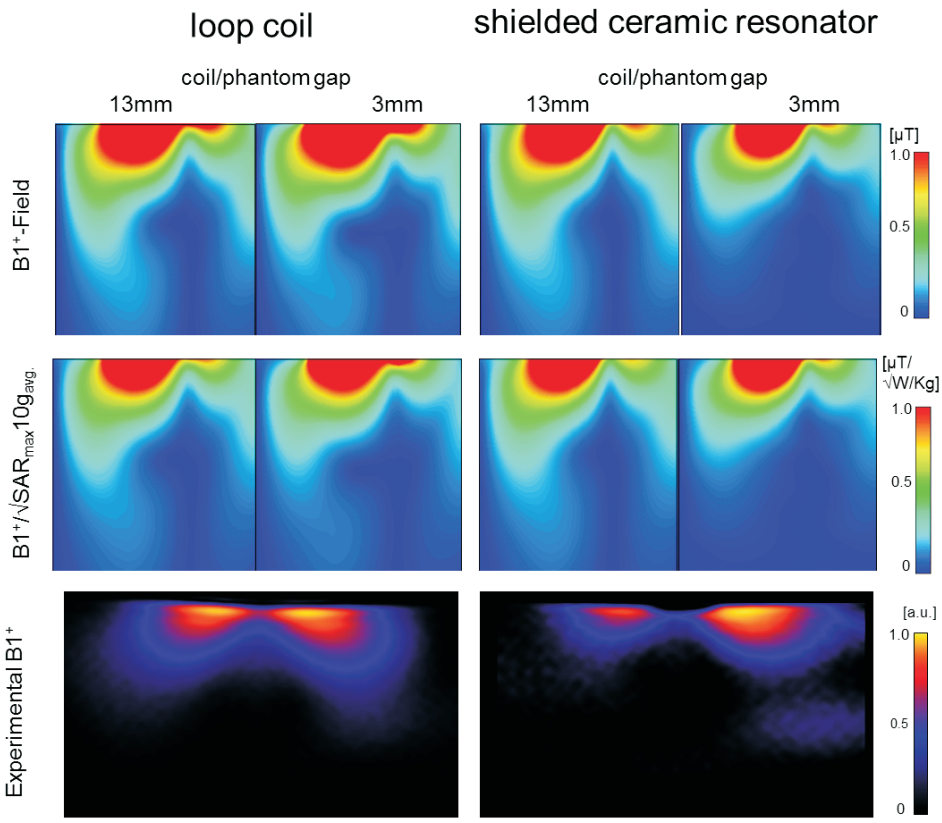

Figure 4.6: (top two rows) Simulated B_1^+ and $B_1^+/\sqrt{\text{SAR}_{10g,\text{max}}}$ distributions for the loop coil and shielded ceramic resonator with 1 Watt (rms) of input power and a uniform phantom. (bottom row) Experimentally-measured B_1^+ maps.

In order to assess the efficiency of the resonators the B_1^+ and maximum SAR ($\text{SAR}_{\text{max,10g}}$) divided by $(B_1^+)^2$ were evaluated along a perpendicular line 35 mm off-centre on the

left-hand side (as shown in Fig. 4.6) of the resonator which corresponds to the region of strongest B_1^+: these results are shown in Figs. 4.7 and 4.8.

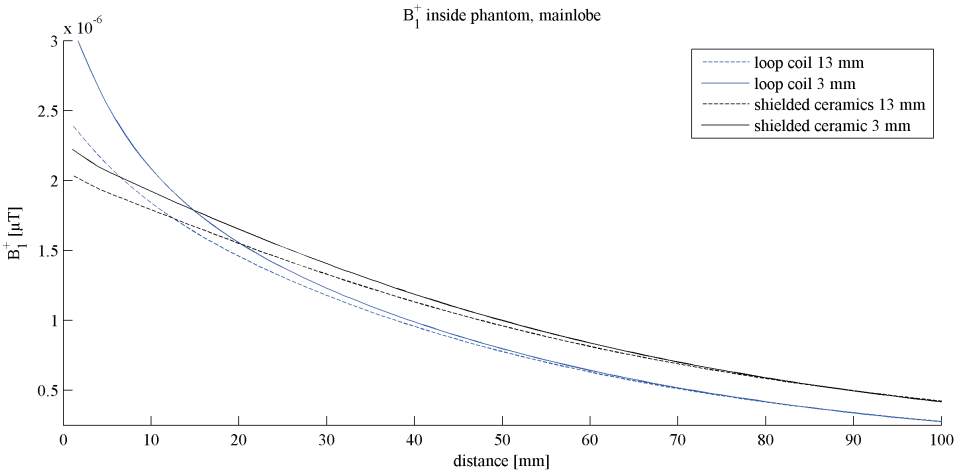

Figure 4.7: Plot of the simulated B_1^+ field as a function of distance from the surface of the resonant element for the loop coil and shielded ceramic for two different spacings (3 mm and 13 mm) of the phantom from the element.

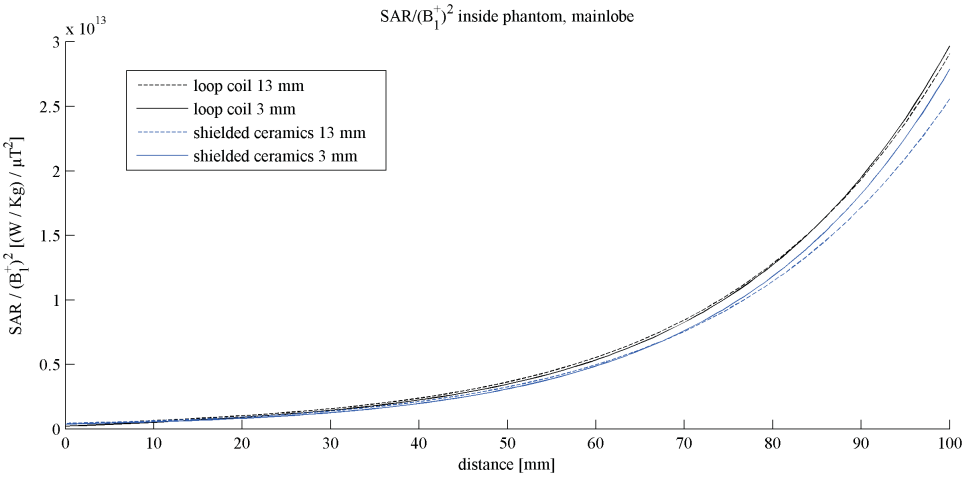

Figure 4.8: Plot of the SAR divided by the square of the B_1^+ field as a function of distance from the two different resonators.

4.3.3. ARRAY ANALYSIS

The coupling between neighboring elements as a function of the inter-element distance was investigated for the shielded ceramic resonator array, with each element spaced 1.5 cm apart, via a series of S_{12}-parameter measurements of a group of three volunteers (body mass index low, medium and high) in the array. The results of the measurement are given in Table 4.2 in terms of mean and standard deviation.

Table 4.2: S-parameter (dB) matrix (mean and standard deviation) for the shielded ceramics array, obtained from three volunteers with different BMIs.

Channel	1	2	3	4	5	6	7	8
1	-15 $\sigma = 4.3$	-16 $\sigma = 1.4$	-27 $\sigma = 5.9$	-39 $\sigma = 7.6$	-25 $\sigma = 3.3$	-39 $\sigma = 11.6$	-35 $\sigma = 7.5$	-36 $\sigma = 2.4$
2		-13 $\sigma = 1.2$	-15 $\sigma = 0.9$	-26 $\sigma = 3.3$	-36 $\sigma = 3.3$	-39 $\sigma = 4.1$	-36 $\sigma = 6.5$	-33 $\sigma = 1.2$
3			-13 $\sigma = 2.2$	-14 $\sigma = 0.5$	-47 $\sigma = 3.7$	-45 $\sigma = 3.8$	-36 $\sigma = 3.3$	-33 $\sigma = 2.4$
4				-23 $\sigma = 6.7$	-47 $\sigma = 10.6$	-44 $\sigma = 5.7$	-39 $\sigma = 8.2$	-33 $\sigma = 2.9$
5					-13 $\sigma = 0.5$	-18 $\sigma = 1.7$	-38 $\sigma = 8.5$	-44 $\sigma = 9.0$
6						-14 $\sigma = 2.5$	-19 $\sigma = 2.4$	-39 $\sigma = 4.1$
7							-16 $\sigma = 3.1$	-19 $\sigma = 1.7$
8								-13 $\sigma = 1.4$

The dual-transmit configuration is only able to provide one degree of freedom in terms of the phase difference between the two sets of anterior and posterior resonators (unlike full phase control for all elements in systems described elsewhere [5, 15]. As described in the methods, an empirical approach was adopted on a subject-specific basis in order to estimate the best relative phase settings. An example is shown in Fig. 4.9, in which the best image quality is produced with zero phase shift between the upper and lower channels. Plots of the simulated B_1^+, SAR and efficiency for the different resonator configurations are given in Fig. 4.10 for an input power of 1 kW for the zero degree phase shift condition shown in Fig. 4.9. It can be seen that the results are very similar for both the loop coil and ceramic resonator. The maximum 10 g averaged SAR was 0.53 W/kg for the loop coil and

0.48 W/kg for the ceramic resonator.

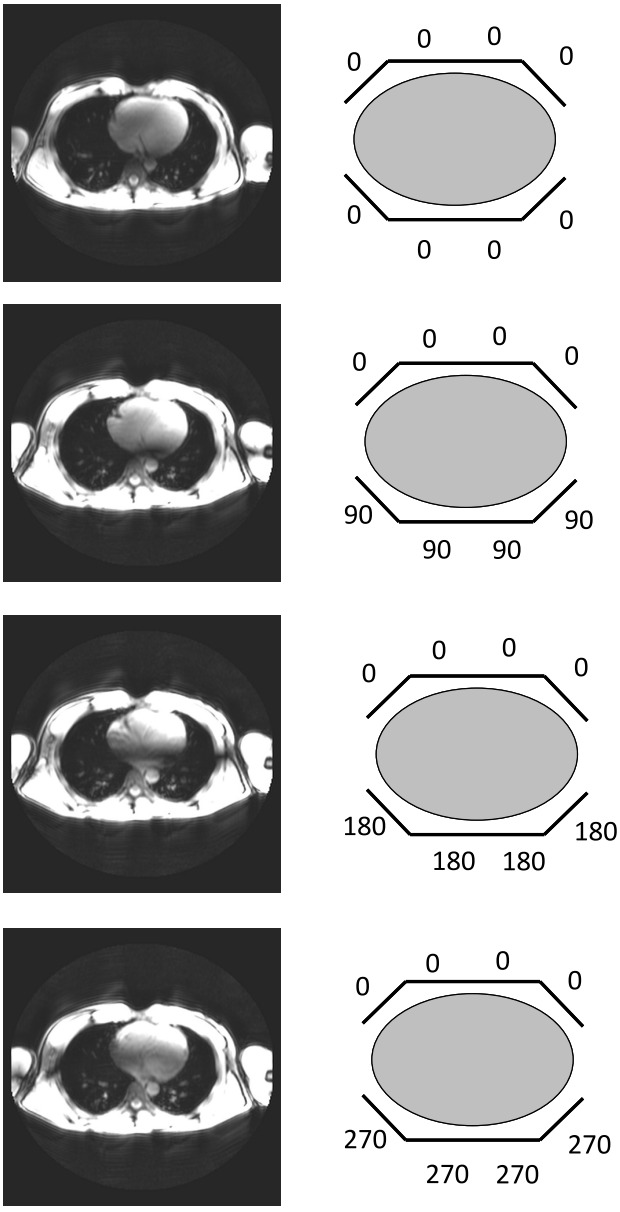

Figure 4.9: Scout images acquired with four different phase shifts between the upper and lower four elements of the array. This very coarse form of B_1-shimming shows that dark bands occur for a 0/90 and 0/180 configuration. The very left and right phase settings shift the dark bands to the right ventricle/atrium.

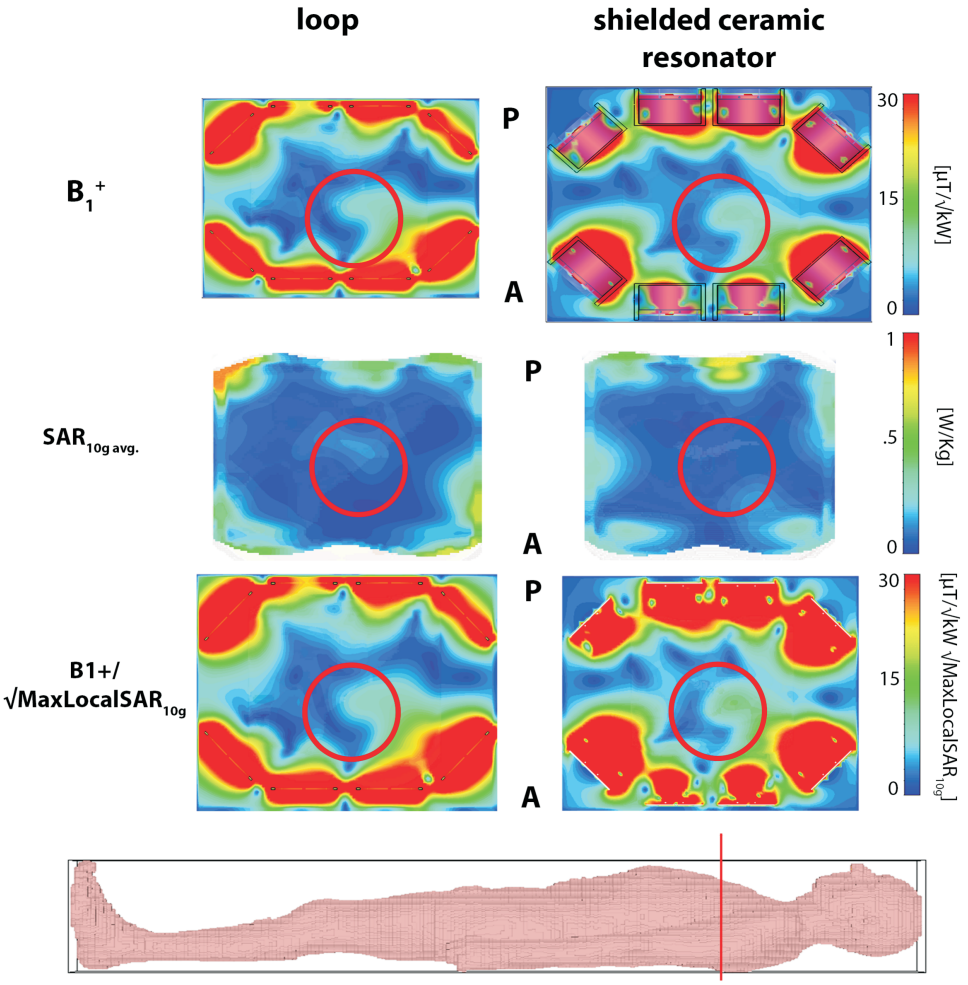

Figure 4.10: Whole body simulations for the loop coil and ceramic resonator with the Gustav model. The phase was set to be equal for all elements. The red circle gives the approximate position of the heart. The position of the cut plane is indicated at the bottom of the figure. The $SAR_{10g,avg}$ figures have been enlarged for better visibility.

4.3.4. IN VIVO RESULTS

Long-axis, short-axis and four-chamber views are shown in Fig. 11, with some views shown for subjects with a low, medium and high BMI. Based on a total power of 20 W time averaged over the whole sequence put out by the system, which corresponds to ~0.27 W/kg for a person with 75 kg body mass (whole body SAR), as the input for the EM simulation, the $SAR_{10g,avg}$ was calculated to be 1.23 W/kg.

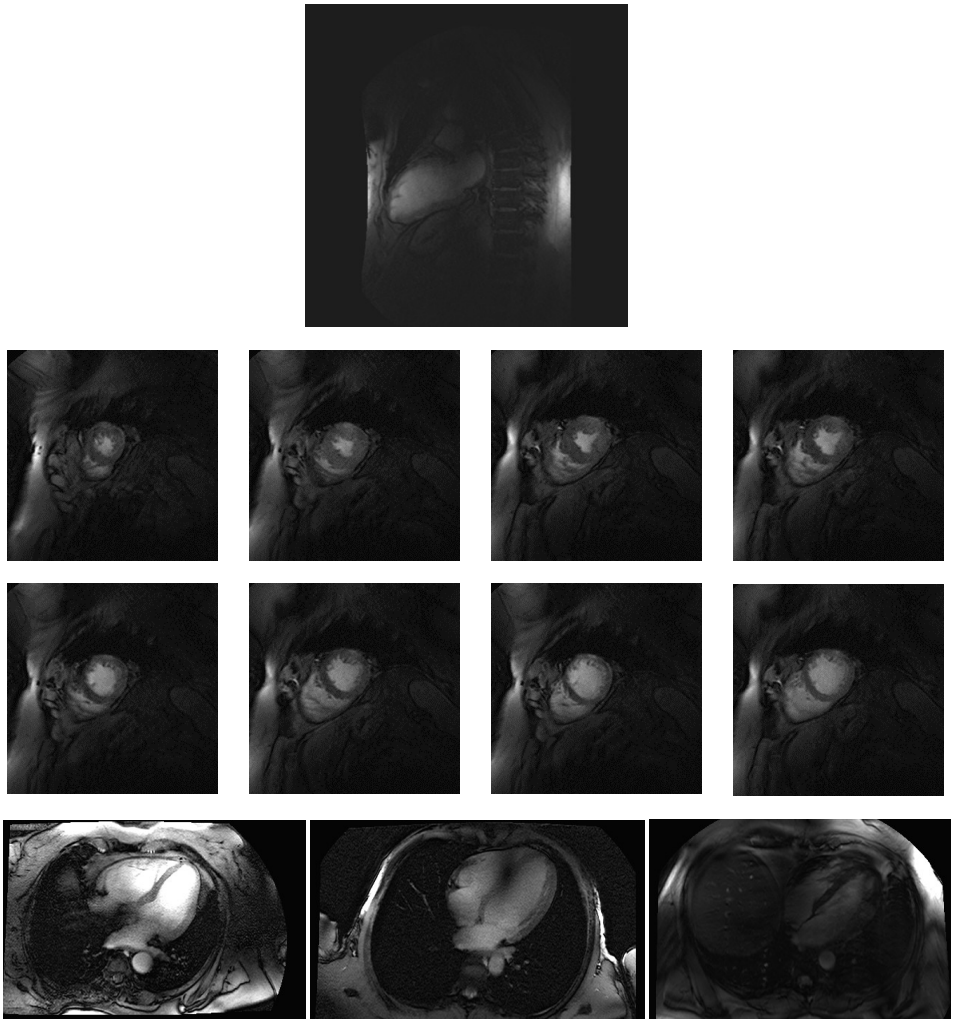

Figure 4.11: Images obtained from a volunteer. (top) two chamber view, (middle two rows) short axis multi-slice images, and (bottom) three four-chamber views obtained from three different volunteers with (BMI low-to-high from left-to-right). Imaging parameters are listed in the main text.

4.4. DISCUSSION

THE results of this work indicate that ceramic resonators can be used as an alternative to loops as surface coil elements at high field strengths. No particular attempt has been made to optimize the size of the resonators in terms of the specific application of cardiac imaging shown here, and so one can anticipate that further improvements could be made. Indeed the use of thinner disks with a larger radius, and/or an elongated rectangular construction, would increase the axial field-of-view. The loop design has been studied for over thirty years, with impressive results shown recently for a very large element-count transmit/receive array for cardiac imaging at 7 T [5]. The basic design of the ceramic resonator has some potential advantages including a smaller number of lumped elements and soldering joints, an inherent high quality factor (>1000 for the ceramic element), and a high degree of isolation between adjacent elements. The fact that the electric field is not concentrated around the lumped elements, but spread over a much larger volume results in a lower SAR for comparable detector sizes for small values of the gap between the body and the coil. However the simulations show for the 3 mm gap case less B_1^+ penetration depth compared to the loop coil. This is most likely due to the fact that the closer the dielectric resonator gets to the phantom the more the boundary condition changed on the contact side of the resonator. One inherent drawback of solid ceramics is of course their relative "inflexibility". Rapid in-house production is usually not possible as special equipment is needed to craft these ceramics, and the required ceramic firing facilities are not standard in academic facilities. There is, however, the possibility to overcome this drawback by using a homogeneous slurry of perovskite powder and a binder such as water as described by Teeuwisse et al. [16]. Those slurries have been shown to achieve even higher relative permittivity of ~300. These slurry can then be put into a plastic former to shape the resonator: simple 3D prototyping capabilities available in most laboratories would then allow the construction of arbitrary conformal shapes.

It should also be noted that these elements can be used as receive-only elements, with very effective detuning of the TE_{01} mode by pin-diode switching using well-established methods [2, 9]. In order to detune the dielectric resonator a conductive loop can either be incorporated into the dielectric resonator, or can be placed on top of the disk, with the diameter of the loop approximately two-thirds that of the resonator, i.e. where the electric field is a maximum. When the conductive loop is complete, this equalizes the electric field around the diameter of the loop, which destroys the modal structure. A pin diode is placed between the ends of the detuning loop, and then can be switched in the normal way.

For this study only two independent RF transmit channels were available, giving relatively minor flexibility in terms of B_1^+ shimming ability. Therefore, one can anticipate that the image quality could be improved by having full phase control over all eight elements, as has been shown by many other groups.

Another drawback for solid ceramic resonator is their weight. With a single element weighing about 1 kg, four resonators put a significant weight on the patient's chest'(one should also note that the weight of a typical commercial cardiac array at 3 T is less than this). However, in our tests all volunteers were comfortable with the extra weight and it did not obstruct breathing: in fact all the volunteers noted that after a couple of minutes they does not feel the extra weight.

Finally, it should be noted that the ceramic disks used in this study are relatively tall, dictated by the relative permittivity of ~170. This means that significant energy is stored within the resonator in the TE_{01} mode. The availability of materials with much higher permittivites, between 1000 and 2000, would allow much thinner DRAs to be designed, in which the TE_{01} mode is intrinsically more "leaky", thus producing a greater magnetic field within the subject. Thinner disks would also reduce the weight considerably.

REFERENCES

[1] S. Aussenhofer and A. Webb. High-permittivity solid ceramic resonators for high-field human mri. *NMR in Biomedicine*, 26(11):1555–1561, 2013.

[2] S. A. Aussenhofer and A. G. Webb. Design and evaluation of a detunable water-based quadrature hem11 mode dielectric resonator as a new type of volume coil for high field mri. *Magnetic Resonance in Medicine*, 68(4):1325–1331, 2012.

[3] A. Christ, W. Kainz, E. G. Hahn, K. Honegger, M. Zefferer, E. Neufeld, W. Rascher, R. Janka, W. Bautz, J. Chen, et al. The virtual family—development of surface-based anatomical models of two adults and two children for dosimetric simulations. *Physics in medicine and biology*, 55(2):N23, 2010.

[4] M. A. Dieringer, W. Renz, T. Lindel, F. Seifert, T. Frauenrath, F. von Knobelsdorff-Brenkenhoff, H. Waiczies, W. Hoffmann, J. Rieger, H. Pfeiffer, et al. Design and application of a four-channel transmit/receive surface coil for functional cardiac imaging at 7t. *Journal of Magnetic Resonance Imaging*, 33(3):736–741, 2011.

[5] A. Graessl, W. Renz, F. Hezel, M. A. Dieringer, L. Winter, C. Oezerdem, J. Rieger, P. Kellman, D. Santoro, T. D. Lindel, et al. Modular 32-channel transceiver coil array for cardiac mri at 7.0 t. *Magnetic Resonance in Medicine*, 72(1):276–290, 2014.

[6] F. Hezel, C. Thalhammer, S. Waiczies, J. Schulz-Menger, and T. Niendorf. High spatial resolution and temporally resolved t 2* mapping of normal human myocardium at 7.0 tesla: an ultrahigh field magnetic resonance feasibility study. *PLoS ONE*, 7:12, 2012.

[7] IEEE. Ieee standard c95.3 recommended practice for measurements and computations of radio frequency electromagnetic fields with respect to human exposure to such fields, 100 khz-300 mhz., 2008.

[8] Int. Soc. Magn. Reson. Med. *J.Y. Lu, X. Zhang, B.K. Rutt, A novel 7 T transmit array using TE01d mode dielectric resonators*, 2013.

[9] D. Kajfez. *Dielectric Resonators*. Institution Engineering & Tech, 1998.

[10] W. Koning, J. Bluemink, E. Langenhuizen, A. Raaijmakers, A. Andreychenko, C. den Berg, P. Luijten, J. Zwanenburg, and D. Klomp. High-resolution mri of the carotid arteries using a leaky waveguide transmitter and a high-density receive array at 7 t. *Magnetic Resonance in Medicine*, 69(4):1186–1193, 2013.

[11] O. Kraff, A. K. Bitz, T. Breyer, S. Kruszona, S. Maderwald, I. Brote, E. R. Gizewski, M. E. Ladd, and H. H. Quick. A transmit/receive radiofrequency array for imaging the carotid arteries at 7 tesla: coil design and first in vivo results. *Investigative radiology*, 46(4):246–254, 2011.

[12] T. Niendorf, A. Graessl, C. Thalhammer, M. A. Dieringer, O. Kraus, D. Santoro, K. Fuchs, F. Hezel, S. Waiczies, B. Ittermann, et al. Progress and promises of human cardiac magnetic resonance at ultrahigh fields: a physics perspective. *Journal of Magnetic Resonance*, 229:208–222, 2013.

[13] A. Raaijmakers, O. Ipek, D. Klomp, C. Possanzini, P. Harvey, J. Lagendijk, and C. Van den Berg. Design of a radiative surface coil array element at 7 t: The single-side adapted dipole antenna. *Magnetic Resonance in Medicine*, 66(5):1488–1497, 2011.

[14] C. Snyder, L. DelaBarre, G. Metzger, P.-F. van de Moortele, C. Akgun, K. Ugurbil, and J. Vaughan. Initial results of cardiac imaging at 7 tesla. *Magnetic resonance in Medicine*, 61(3):517–524, 2009.

[15] C. Snyder, L. DelaBarre, S. Moeller, J. Tian, C. Akgun, P.-F. Van de Moortele, P. Bolan, K. Ugurbil, J. Vaughan, and G. Metzger. Comparison between eight-and sixteen-channel tem transceive arrays for body imaging at 7 t. *Magnetic Resonance in Medicine*, 67(4):954–964, 2012.

[16] W. Teeuwisse, W. Brink, K. Haines, and A. Webb. Simulations of high permittivity materials for 7 t neuroimaging and evaluation of a new barium titanate-based dielectric. *Magnetic Resonance in Medicine*, 67(4):912–918, 2012.

[17] C. Thalhammer, W. Renz, L. Winter, F. Hezel, J. Rieger, H. Pfeiffer, A. Graessl, F. Seifert, W. Hoffmann, F. von Knobelsdorff-Brenkenhoff, et al. Two-dimensional sixteen channel transmit/receive coil array for cardiac mri at 7.0 t: Design, evaluation, and application. *Journal of Magnetic Resonance Imaging*, 36(4):847–857, 2012.

[18] S. G. van Elderen, M. J. Versluis, A. G. Webb, J. J. Westenberg, J. Doornbos, N. B. Smith, A. de Roos, and M. Stuber. Initial results on in vivo human coronary mr angiography at 7 t. *Magnetic Resonance in Medicine*, 62(6):1379–1384, 2009.

[19] S. G. van Elderen, M. J. Versluis, J. J. Westenberg, H. Agarwal, N. B. Smith, M. Stuber, A. de Roos, and A. G. Webb. Right coronary mr angiography at 7 t: A direct quantitative and qualitative comparison with 3 t in young healthy volunteers 1. *Radiology*, 257(1):254–259, 2010.

[20] J. T. Vaughan, C. J. Snyder, L. J. DelaBarre, P. J. Bolan, J. Tian, L. Bolinger, G. Adriany, P. Andersen, J. Strupp, and K. Ugurbil. Whole-body imaging at 7t: Preliminary results. *Magnetic resonance in Medicine*, 61(1):244–248, 2009.

[21] F. von Knobelsdorff-Brenkenhoff, T. Frauenrath, M. Prothmann, M. A. Dieringer, F. Hezel, W. Renz, K. Kretschel, T. Niendorf, and J. Schulz-Menger. Cardiac chamber quantification using magnetic resonance imaging at 7 tesla—a pilot study. *European radiology*, 20(12):2844–2852, 2010.

[22] F. von Knobelsdorff-Brenkenhoff, V. Tkachenko, L. Winter, J. Rieger, C. Thalhammer, F. Hezel, A. Graessl, M. A. Dieringer, T. Niendorf, and J. Schulz-Menger. Assessment of the right ventricle with cardiovascular magnetic resonance at 7 tesla. *J Cardiovasc Magn Reson*, 15(23):10–1186, 2013.

[23] A. Webb. Visualization and characterization of pure and coupled modes in water-based dielectric resonators on a human 7t scanner. *Journal of Magnetic Resonance*, 216:107–113, 2012.

[24] H. Wen, F. A. Jaffer, T. J. Denison, S. Duewell, A. S. Chesnick, and R. S. Balaban. The evaluation of dielectric resonators containing h_2o or d_2o as rf coils for high-field mr imaging and spectroscopy. *Journal of Magnetic Resonance, Series B*, 110(2):117–123, 1996.

[25] L. Winter, P. Kellman, W. Renz, A. Gräßl, F. Hezel, C. Thalhammer, F. von Knobelsdorff-Brenkenhoff, V. Tkachenko, J. Schulz-Menger, and T. Niendorf. Comparison of three multichannel transmit/receive radiofrequency coil configurations for anatomic and functional cardiac mri at 7.0 t: implications for clinical imaging. *European radiology*, 22(10):2211–2220, 2012.